Enhancement of the Thermal. Polarization of Water via Heat Flux and Dipole Moment Dynamic Correlations

3 AUTHORS, INCLUDING:

Jeff Armstrong
Science and Technology Facilities Council
11 PUBLICATIONS **25** CITATIONS

SEE PROFILE

Anders Lervik
Norwegian University of Science and Techno…
**19** PUBLICATIONS **155** CITATIONS

SEE PROFILE

Enhancement of the Thermal Polarization of Water via Heat Flux and Dipole Moment Dynamic Correlations

Jeff Armstrong,*,[†] Anders Lervik,[†],* and Fernando Bresme*,[†],[‡]

[†]Department of Chemistry, Imperial College London, SW7 2AZ London, United Kingdom
[‡]Department of Chemistry, Norwegian University of Science and Technology, Trondheim, Norway

ABSTRACT: It has been recently shown that liquid water polarizes as a response to a temperature gradient. This polarization effect can be significant for temperature gradients that can be achieved at micro and nanoscales. In this paper we investigate the dependence of the polarization response of liquid and supercritical water at different thermodynamic conditions using both equilibrium and nonequilibrium molecular dynamics simulations for the extended point charge water model. We find that the thermal polarization features a nonmonotonic behavior with temperature, reaching a maximum response at specific thermodynamic states. We show that the thermal polarization is maximized when the density of states of the heat flux and dipole moment correlation functions feature the strongest overlap. The librational modes of water are shown to play an important role in determining this behavior as well as the heat transport mechanism in water. The librational frequencies show a significant dependence with temperature and pressure. This dependence provides a microscopic mechanism to explain the observed maximization of the thermal-polarization effect. Our work provides new microscopic insights on the mechanism determining the orientation of polar fluids under thermal gradients, as well as new strategies to maximize their orientation by manipulating the dynamic correlations between the heat flux and the sample dipole moment.

$$\mathbf{E} = \left(1 - \frac{1}{\varepsilon_r}\right)\frac{L_{pq}}{L_{pp}}\frac{\nabla T}{T}$$
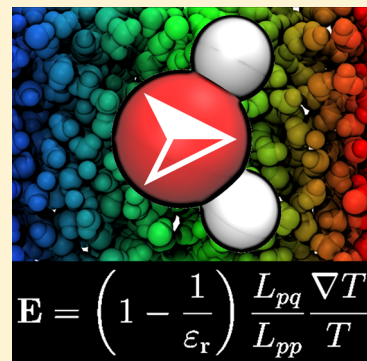
I. INTRODUCTION

Heat dissipation plays an important role in many problems of technological and industrial interest. The development of devices that convert the heat dissipated by machines, at difference length scales (from macro to nano), into other forms of usable energy is an objective of clear practical significance. The thermal gradients associated with heat dissipation processes can induce a number of coupled effects: concentration gradients in fluid mixtures (thermodiffusion)[1−3] or particle motion in suspensions (thermophoresis).[4−7] These effects influence the composition of oil reservoirs and have been employed to design nanoscale thermophoretic devices, with applications in bioanalytical assays.[8] All these phenomena belong to a general class of nonequilibrium processes, which were observed for the first time by Ludwig and Soret in the 19th century.[9] Despite the practical and scientific relevance of this effect, a general theory that can explain all these phenomena in a variety of systems is still outstanding, even in the apparently simpler case of ionic solutions.[10]

In addition to the vectorial transport phenomena discussed above, it has been shown that thermal gradients can induce a preferred orientation in water.[11] Related effects had been observed in early experiments by Lehman, shortly after the discovery of liquid crystals (LC), who showed that the average molecular orientation of the anisotropic LC can be modified by applying a thermal gradient.[12] It has also been shown very recently that thermal gradients induce long-range order in one-dimensional dipole chains,[13] a result that is consistent with the theory and simulations discussed in ref 11. In the particular case

of water, a highly polar fluid, it was demonstrated that the reorientation leads to an electrostatic field, which scales with the magnitude of the thermal gradient. A nonequilibrium analysis of this problem shows that the field varies linearly with the thermal gradient and inversely with temperature and also depends on the polarity of the liquid through the dielectric permittivity and the so-called phenomenological coefficients, which measure the dipole moment correlation time of the sample and the coupling between the heat flux and the polarization. This thermal-polarization effect in water has been confirmed in subsequent computer simulation studies of the modified central force model,[14] and more recently using one of the most accurate empirical water models, the extended single point charge model (SPC/E).[15] This simulation work along with the nonequilibrium theory clearly show the generality of this phenomenon. Recently, we have also shown that nonpolar molecules adopt a preferred orientation under a thermal gradient, and a correlation between this phenomenon and the Soret effect discussed above has also been established.[16]

We have shown in previous work that water features a strong thermal-polarization response. Fields of $\sim 10^6$ V/m can be generated with thermal gradients of about $\sim 10^8$ K/m. The latter gradients are strong for macroscopic standards, but gradients between 10^5 and 10^9 K/m can be easily generated at the micro- and nanoscales,[4,17,18] making the thermal-polarization response a

viable effect. So far, the investigation of the thermal-polarization response of water has focused on specific thermodynamic states, although the dependence of this response with the molecular geometry and mass distribution has also been considered.[15] In this article we investigate the thermal-polarization response of water at different thermodynamic conditions by performing nonequilibrium molecular dynamics simulations of the SPC/E model. This analysis is important to find regions in the thermodynamic phase diagram where the thermal polarization can be maximized, as well as to establish a connection between the magnitude of the nonequilibrium response and the variation of thermodynamic and dynamical properties with pressure and temperature, including the anomalous behavior of these properties. Attaining a good microscopic understanding of the nonequilibrium physicochemical behavior of water is essential to advance in the development of energy conversion approaches that exploit the thermal-polarization effect.

Our paper is structured as follows. We first discuss the theoretical background behind the thermal-polarization effect in section I. The methodology and model details are then discussed in section II. In section III we present the main results obtained in this work. We discuss the dependence of the polarization with the thermodynamic state point, provide estimates of the phenomenological coefficients that determine the strength of the thermal polarization, and analyze the dynamic correlations of the heat flux and the sample dipole moment. A final section (IV) containing our main conclusions and final remarks closes the paper.

II. BACKGROUND AND METHODOLOGY

Background. The existence of thermal polarization in water was reported for the first time in ref 11 using a modified version of the central force model of water.[14,19] Nonequilibrium thermodynamics (NET) has been used to derive an equation connecting the polarization field and the thermal gradient.[11] The NET description is based on the entropy production of the system, σ, which for an isotropic polar fluid subjected to a temperature gradient is given by[11]

$$\sigma = -\frac{1}{T}\frac{\partial \mathbf{P}}{\partial t} \cdot (\mathbf{E}_{eq} - \mathbf{E}) - \frac{1}{T^2}\mathbf{J}_q \cdot \nabla T \tag{1}$$

where $\mathbf{P}$ is the polarization, $\mathbf{E}$ is the electrostatic field, $\mathbf{J}_q$ is the heat flux, and T is the temperature. Furthermore, the equilibrium field, $\mathbf{E}_{eq}$, is given by $\mathbf{E}_{eq} = \mathbf{P}/(\chi_e \varepsilon_0)$, where $\chi_e = \varepsilon_r - 1$ is the electric susceptibility, ε_r is the relative dielectric constant, and ε_0 is the vacuum permittivity. From the entropy production, the following two linear force-flux relations can be obtained,[11]

$$\frac{\partial \mathbf{P}}{\partial t} = -\frac{L_{pp}}{T}(\mathbf{E}_{eq} - \mathbf{E}) - \frac{L_{pq}}{T^2}\nabla T \tag{2}$$

$$\mathbf{J}_q = -\frac{L_{qp}}{T}(\mathbf{E}_{eq} - \mathbf{E}) - \frac{L_{qq}}{T^2}\nabla T \tag{3}$$

where $L_{\alpha\beta} = L_{\beta\alpha}$ are the phenomenological coefficients. In the stationary state, and in the absence of free charges where $\mathbf{P} = -\varepsilon_0\mathbf{E}$, eq 2 can be rearranged to give[11]

$$\mathbf{E} = \left(1 - \frac{1}{\varepsilon_r}\right)\frac{L_{pq}}{L_{pp}}\frac{\nabla T}{T} \tag{4}$$

According to eq 4 the electrostatic field associated to the polarization of the sample is proportional to the temperature gradient. Furthermore, the strength of the thermal-polarization effect is determined by the ratio of the phenomenological coefficients, L_{pq}/L_{pp}. The coefficient L_{pq}, which can be positive or negative, measures the coupling of the heat flux and the polarization. L_{pp} on the other hand is always positive and is related to the Debye relaxation time as discussed by de Groot and Mazur.[9]

When the temperature gradient is absent and the electric field is constant, we can solve the first phenomenological linear relation, eq 2,

$$\frac{\partial \mathbf{P}}{\partial t} = -\frac{L_{pp}}{\kappa T}(\mathbf{P} - \kappa\mathbf{E}) \tag{5}$$

and obtain the polarization as

$$\mathbf{P}(t) = \kappa\mathbf{E}(1 - e^{-t/\tau}) \tag{6}$$

where $\kappa = \chi_e\varepsilon_0$ and the characteristic relaxation time, τ, is given by[9]

$$L_{pp} = \frac{\kappa T}{\tau} \tag{7}$$

Equation 7 provides a route to estimate L_{pp} within the approximations used in the Debye model. The coupling coefficient L_{pq} can then be extracted from eq 4 using as input the temperature gradient, the electrostatic field and the dielectric constant calculated from computer simulations.

In the following section we discuss the simulation approaches employed in this work.

Nonequilibrium Molecular Dynamics Computer Simulations. We have employed the rigid and nonpolarizable SPC/E force field[20] to model the water molecules. This model reproduces the anomalous increase of the thermal conductivity of water,[21] and it provides an accurate representation of the fluid properties of water. Moreover, we have recently shown that the SPC/E model features the thermal-polarization effect.[15] Hence this model provides a good basis to perform a systematic investigation of the dependence of the thermal-polarization effect with the thermodynamic conditions.

All the simulations reported in this work were performed using the molecular dynamics software package LAMMPS.[22] The electrostatic interactions arising from the SPC/E partial charges were computed via the original implementation of the Wolf method.[23] We note that other implementations are possible, which remove the force discontinuity of the Coulombic forces at the cutoff.[24] We have shown recently that these two implementations produce the same results when applied to systems away from equilibrium.[15] Within the Wolf method the energy of a particle with charge q_i due to the presence of other charged particles is

$$U_{elec} = \frac{1}{2(4\pi\varepsilon_0)}\sum_{i,j\neq i}^{N}\left(\frac{q_iq_j\,\mathrm{erfc}(\alpha r_{ij})}{r_{ij}} - \frac{q_iq_j\,\mathrm{erfc}(\alpha r_c)}{r_c}\right)$$
$$- \frac{1}{4\pi\varepsilon_0}\sum_{i=1}^{N}q_i^2\left(\frac{\mathrm{erfc}(\alpha r_c)}{2r_c} + \frac{\alpha}{\sqrt{\pi}}\right) \tag{8}$$

where α is a parameter that controls the convergence of the Coulombic potential, normally the parameter that controls the width of the Gaussian in the traditional Ewald summation method. In this study we used $\alpha L \approx 7.2$, where L is the length of the shortest vector in the simulation box, $\mathbf{L} = L_y = L_x$. The cutoff for the Coulombic and dispersion interactions was set to $r_c = 11$ Å.

The thermal gradient was set up by thermostating the edges and the center of the simulation box. In this work we have employed a simplified thermostat where the velocities are rescaled to the desired temperature, hot (T_h) or cold (T_c), by using a suitable rescaling factor, ξ, which is applied on the atomic velocities. The scaling factor is given by $\xi = (K_D/K)^{1/2}$, where K is the instantaneous kinetic energy of the particles within the thermostated region and K_D is the kinetic energy corresponding to the desired temperature. A sketch of the simulation cell is shown in Figure 1. We note that the velocity rescaling modifies
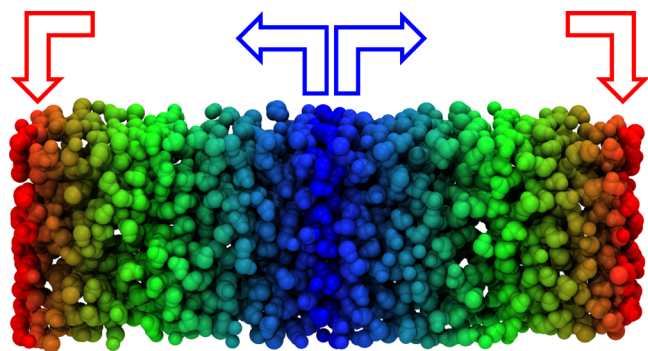

Figure 1. Schematic of the standard NEMD simulation cell, showing the hot (at the edges) and the cold thermostats (in the middle). The color scale from red (hot) to blue (cold) illustrates the thermal gradient in the simulation box.

the total momentum of the system. To eliminate the resulting barycentric velocity, the momentum of the whole system is reset to zero after each rescaling. We note that other choices for the thermostats, e.g., a canonical thermostat, are possible.[21] Advancing the discussion below we find that, within the accuracy of our NEMD approach, the thermal conductivities are insensitive to the details of the thermostat employed.

All the NEMD simulations consisted of 1500 SPC/E water molecules arranged in a periodic orthorhombic box with box dimensions $\{L_x, L_x, 3L_x\}$. The length L_x was in the range 25.28–31.92 Å, to account for different average densities. The simulation time step was set to 2.0 fs in all cases. To simulate the desired thermodynamic states via NEMD, we first performed equilibrium NPT simulations using a Nosé–Hoover barostat to ascertain the average volume, $\langle V \rangle$ to be used in the NEMD simulation. An initial 0.5 ns equilibration period was performed followed by a production run lasting 1.0 ns. A configuration with the aforementioned box aspect ratio was then generated and thermalized/equilibrated for 0.4 ns in the NVT ensemble using a Nosé–Hoover thermostat. The average temperature in these NVT/NPT runs was set to $T = (T_h + T_c)/2$. Then the NEMD simulation was initiated by activating the two thermostats, and a thermal gradient along the z-axis was established. The thermostats were applied *every time step*. The width of the thermostats was chosen to span 4 Å along the z-axis and as indicated above (Figure 1), the thermostats were positioned at the edges and in the middle $(L_z/2)$ of the simulation box. As water has a high thermal diffusivity, stationary temperature profiles can be generated in just a few tens of picoseconds for densities typical of liquids (see, e.g., ref 25 for an analysis of this question). Our NEMD simulation, however, involved much longer production runs to gather statistics, typically 3 ns were performed and 3×10^5 configurations were used to obtain statistical averages of the temperature, density and polarization profiles.

The dielectric constant, ε_r, appearing in eq 4 was computed from equilibrium simulations in the canonical ensemble (NVT) using the fluctuation formula,[26]

$$\varepsilon_r - 1 = \frac{4\pi[\langle \mathbf{P}^2 \rangle - \langle \mathbf{P} \rangle^2]}{3Vk_BT\varepsilon_0} \tag{9}$$

where $\mathbf{P} = \Sigma_{i=1}^{N} q_i \mathbf{r}_i$ is the dipole moment of the whole simulation box, V is the box volume, and k_B is the Boltzmann constant. The validity of this equation to compute the dielectric constant using the Wolf potential has been discussed in ref 27. We have also tested this equation in the context of nonequilibrium simulations of the SPC/E water model.[15] We found that the changes in the dielectric constant, for typical thermal-polarization fields achievable in the simulations are rather small (≈ 2 units). Because the dielectric constants we consider here are in the range 6–40, these changes have a minor effect in the estimates of the phenomenological coefficients as the factor $(1 - 1/\varepsilon_r)$ appearing in eq 4 is in all cases close to 1. Furthermore, the dielectric constants obtained from the full Ewald treatment or the Wolf approach are equal within the error of the simulations. All the dielectric constants employed in this work were computed using the Ewald summation method.

III. RESULTS AND DISCUSSION

Before presenting our results for the thermal polarization of SPC/E water, we assess the accuracy of the thermostating algorithm employed in this work by computing the thermal conductivity, λ, for selected thermodynamic states. The thermal conductivity of the SPC/E model has been investigated by several authors. Most of these works show that the SPC/E model overestimates the thermal conductivity of water at 300 K and 1 g/cm^3 density.[28−31] We have recently reported an extensive investigation of the thermal conductivity of water using both the SPC/E and TIP4P-2005 models, covering a wide range of thermodynamic states.[21] We found that the SPC/E model is fairly accurate. It reproduces the increase of the thermal conductivity with temperature and provides a quantitative prediction of the thermal conductivity at high temperatures and low densities. Hence we use the results obtained in ref 21 as a reference to test our implementation of the thermostating method. The thermal conductivity was obtained from Fourier's law, $J_q = -\lambda \nabla T$, where the heat flux J_q is given by the continuity equation (see, e.g., refs 32 and 33)

$$J_q \equiv J_U = \frac{\pm \Delta K}{2\delta t A} \tag{10}$$

where J_q and J_U are the heat and internal energy fluxes (in the z-direction), which are identical in the absence of a mass flux. ΔK is the average amount of kinetic energy added (+) or removed (−) from the hot and cold thermostat, respectively, over the course of a simulation. δt is the simulation time step and A is the simulation box cross sectional area. Because the thermostating algorithm does not modify the atomic coordinates upon addition or withdrawal of kinetic energy, the change in kinetic energy gives directly the change in internal energy required to compute the heat flux.

In these test simulations we employed a cutoff of 9 Å for the dispersion interactions, and the electrostatic interactions were computed with the particle–particle particle-mesh method.[34] The simulations involved 1500 molecules arranged in a simulation box with the same aspect ratio as discussed in the Background and Methodology section. The thermal conductiv-

C

dx.doi.org/10.1021/jp408485d | *J. Phys. Chem. B* XXXX, XXX, XXX–XXX

ities were computed from temperature profiles obtained over trajectories spanning 1−2 ns. Figure 2 shows our results for the
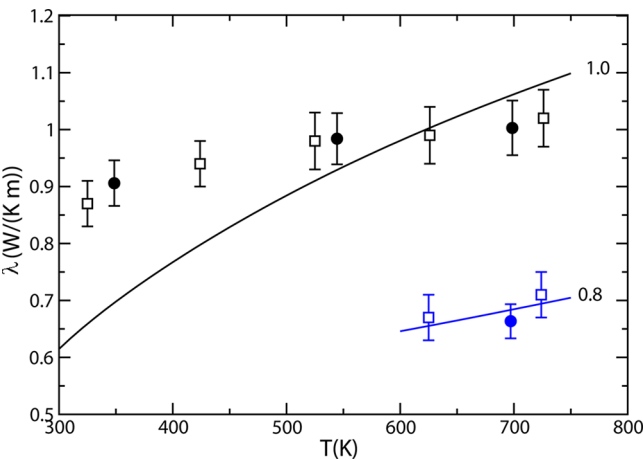

Figure 2. Thermal conductivity of the SPC/E model as a function of temperature and densities, 1 and 0.8 g/cm^3. The full symbols are results obtained in this work, and the open symbols are taken from ref 21. The full lines are the results from the correlation formula proposed in ref 35.

thermal conductivity. The simple thermostating scheme implemented here predicts thermal conductivities in very good agreement with previous work.[21] As observed in that work, the agreement with the experimental results improves at high temperature.

We have validated our NEMD approach above. We proceed in the following to discuss the main results obtained in this work. For the main portion of the study, each chosen thermodynamic state required three NEMD simulations with different temperature gradients. These three simulations where used to extract information on the ratio of the phenomenological coefficients. For each simulation we extracted the temperature, density and electrostatic field profiles, by dividing the simulation box into 200 bins in the direction of the temperature gradient. Figure 3 shows the thermodynamic states investigated in this work, which include liquid and supercritical states (Table 1 compiles information on the simulation conditions). We have also represented in the inset in this figure typical temperature and density gradients, which are used to construct the corresponding equations of state. Our results show that to a good approximation the equations of state obtained with different gradients fall on the same line despite the fact that different thermal gradients lead to different degrees of polarization. This result shows that, within the accuracy of our simulations, the equations of state are not sensitive to the varying polarization across the different simulations.

To quantify the electrostatic field induced by the thermal gradients, we performed a numerical integration of the charge density, ρ_q, using Gauss' theorem,

$$E(z) = \frac{1}{\varepsilon_0} \int_{-\infty}^{z} \rho_q(z') \, dz' \tag{11}$$

The charge density was calculated using the density of the species, $\rho_\alpha(z)$, and the corresponding charge, q_α, $\rho_q(z) = \rho_O(z)q_O + \rho_H(z)q_H$. To further improve the statistics, the simulation data were then folded, taking advantage of the mirror symmetry of the simulation cell around the center. The electric field of a representative thermodynamic state as a function of the applied
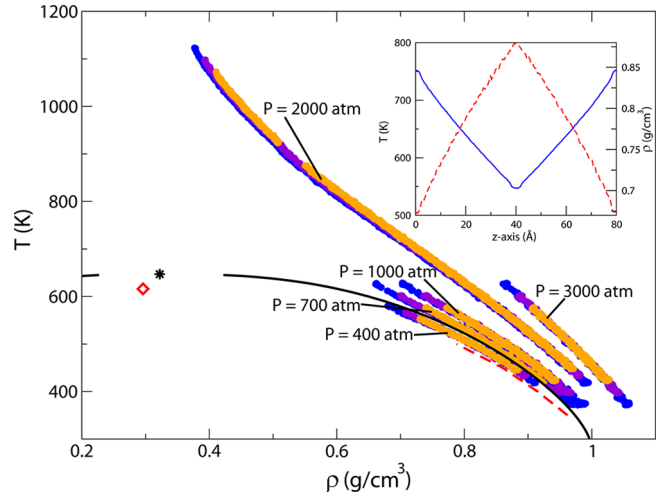

Figure 3. Equations of state obtained from NEMD simulations at different pressures. The applied temperature gradients are represented from largest to smallest with orange, purple, and blue circles, respectively. The full and dashed lines represent the liquid branches of water for experiments[36] and SPC/E,[37] respectively. The star and the diamond represent the experimental[36] and SPC/E[38] critical points, respectively. The inset shows representative temperature and density profiles for P = 2000 atm and $(T_H, T_c) = (750, 550)$ K.

Table 1. Temperatures and Box Lengths Used in the Simulations Performed in This Work

T_H (K)	T_c (K)	P (bar)	L_z (Å)	$L_x = L_y$ (Å)
553	447	400	79.14	26.38
565	434	400	79.14	26.38
579	420	400	79.14	26.38
575	425	700	78.21	26.07
600	400	700	78.21	26.07
625	375	700	78.21	26.07
575	425	1000	77.52	25.84
600	400	1000	77.52	25.84
625	375	1000	77.52	25.84
550	450	2000	75.84	25.28
565	435	2000	75.84	25.28
580	420	2000	75.84	25.28
650	500	2000	77.811	25.937
675	475	2000	77.811	25.937
700	450	2000	77.811	25.937
725	575	2000	80.16	26.72
750	550	2000	80.16	26.72
775	525	2000	80.16	26.72
800	650	2000	82.98	27.66
825	625	2000	82.98	27.66
850	600	2000	82.98	27.66
875	725	2000	86.22	28.74
900	700	2000	86.22	28.74
925	675	2000	86.22	28.74
1075	925	2000	95.76	31.92
1100	900	2000	95.76	31.92
1125	875	2000	95.76	31.92
575	425	3000	74.70	24.9
600	400	3000	74.70	24.9
625	375	3000	74.70	24.9

temperature gradient is shown in Figure 4. Similar behavior was observed for other thermodynamic states.
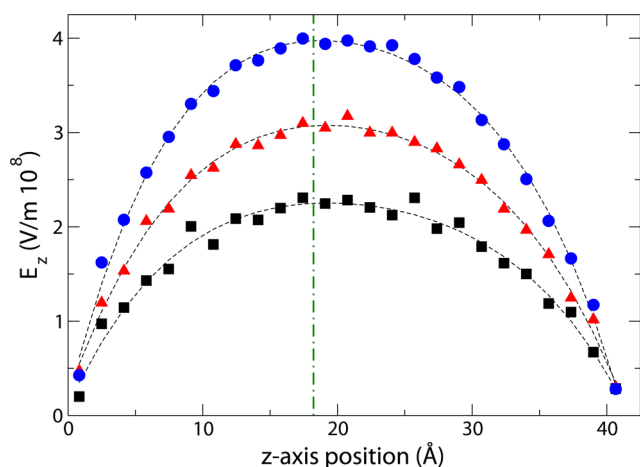
Figure 4. Variation of the electric field (E_z) along the simulation box at average temperature, 725 K, and average pressure, 2000 atm. The hot and cold thermostats are located at 0 and 41.5 Å, respectively. Squares, triangles, and circles represent results at different thermal gradients, 3.62, 4.82, and 6.03 K/Å respectively, and the lines are a guide to the eye. The vertical line indicates thermodynamic states at the same temperature, 721.5 K, which are used to quantify the dependence of the field with the thermal gradient strength (Figure 5).

The parabolic shape of the electrostatic field along the simulation box has been explained before in ref 11. This shape is a result of the boundary conditions that the field must fulfill at the thermostats, where the field changes sign.

The electrostatic field associated to the water polarization increases with the thermal gradient strength (Figure 5). The electrostatic fields are positive for all the thermodynamic states investigated here, indicating that the water dipole points toward the hot region, i.e., SPC/E water features thermophilic orientation under these thermodynamic conditions.

According to nonequilibrium thermodynamics, eq 4, the field increases with the thermal gradient, and the magnitude of the field depends on the temperature of the system, the ratio of the phenomenological coefficients, L_{pq}/L_{pp}, and the dielectric permittivity. To quantify the ratio of the coefficients, we consider the same thermodynamic state, i.e., the same temperature/pressure/density, for systems with different applied thermal

gradients. To achieve this, the simulations were performed in such a way that the thermal gradients cross at the temperature of interest (see, e.g., Figure 10 in ref 15).

Nonequilibrium thermodynamics predicts a linear increase of the field with the thermal gradient. This linear dependence is fulfilled by our simulations (see Figure 5 for a representative result for the 2000 atm isobar), making it possible to calculate the slope of eq 4, $(1 - 1/\varepsilon_r)(L_{pq}/L_{qq})(1/T)$. To extract the ratio L_{pq}/L_{pp} from the slope, we used the dielectric constants obtained from equilibrium simulations in the *NVT* ensemble (Table 2).

Table 2. Structural and Thermodynamic Properties of the SPC/E Water Model for the Different Thermodynamic States Investigated in This Work[a]

T (K)	P (atm)	ρ (g/cm^3)	S_{tet}	N_{HB}	D (10^{-5} cm^2/s)	ε_r	τ (ps)
500	2000	0.931	0.129	2.81	18.2	35.3	1.13
575	2000	0.864	0.137	2.50	26.7	26.3	0.78
650	2000	0.793	0.145	2.19	35.8	19.8	0.50
725	2000	0.717	0.153	1.90	46.1	14.9	0.33
800	2000	0.641	0.160	1.62	60.2	11.0	0.24
1000	2000	0.468	0.176	1.05	102.3	5.8	0.16

[a]ρ represents the density, S_{tet} is the tetrahedral order parameter obtained from eq 12. Typical values for the order parameters vary from $S_{tet} \sim 0.012$ and 0.1 for SPC/E hexagonal ice and SPC/E water at 300 K and 1 bar, to 0.15, for a typical Lennard-Jones liquid, where there are no hydrogen bonding correlations present. N_{HB} is the number of hydrogen bonds per molecule (see main text for details on the criterion employed to calculate this quantity), D is the diffusion coefficient, ε_r is the dielectric constant, and τ is the Debye relaxation time.

Our simulations show two very distinctive behaviors. At constant temperature (500 K) the ratio of the phenomenological coefficients, L_{pq}/L_{pp}, decreases with pressure, going from 5.5 V at 400 atm to 2.0 V at 3000 atm, showing that the thermal polarization is weakened by pressure. The behavior at constant pressure is more complex and considerably more interesting. We find that the ratio of phenomenological coefficients features a minimum at about 725 K (Figure 5 right), indicating an enhancement of the thermal polarization at specific thermody-
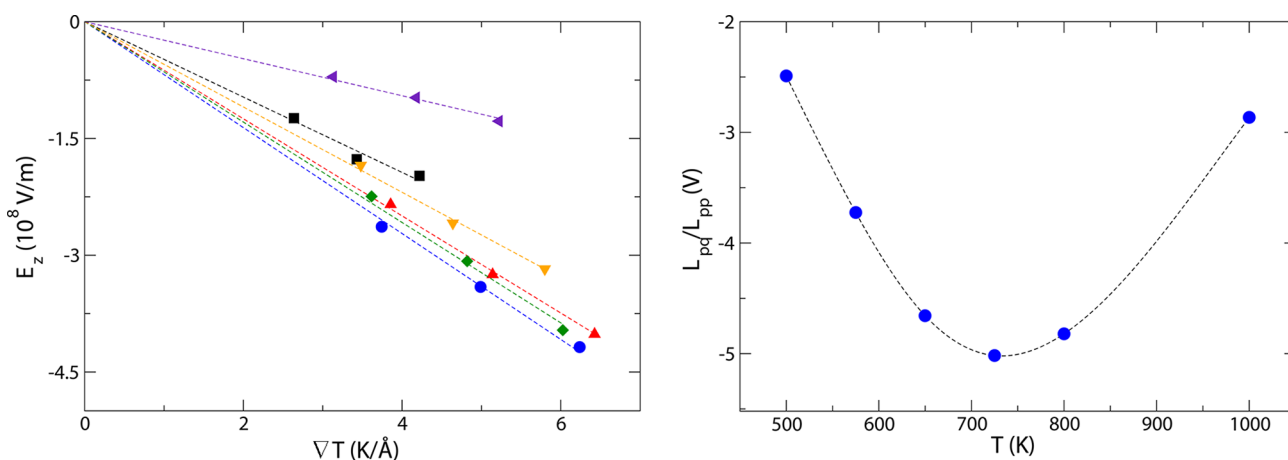

Figure 5. (Left) dependence of the electrostatic field (E_z) with the thermal gradient strength (∇T). The dashed lines represent the linear fitting used to extract the ratio of the phenomenological coefficients, L_{pq}/L_{qq} (eq 5). The temperatures shown are 500 K (black), 575 K (red), 650 K (blue), 725 K (green), 800 K (orange), and 1000 K (purple). This color key will be used for the remainder of the text. All the data correspond to the 2000 atm isobar. (Right) resulting ratio of phenomenological coefficients for this data (obtained from eq 4) plotted versus temperature.

E

dx.doi.org/10.1021/jp408485d | *J. Phys. Chem. B* XXXX, XXX, XXX–XXX

namic states. It is well-known that many thermodynamic and transport properties of water feature a nonmonotonic behavior with temperature (e.g., density, isothermal compressibility, thermal conductivity or diffusion coefficient). Although a full rigorous microscopic interpretation is still lacking, it is well accepted that the modification of the hydrogen bonding structure must play a role in defining such behavior. The minimum in the ratio L_{pq}/L_{pp} is a new addition to the large number of water properties that feature a nonmonotonic behavior with temperature. In the following we investigate the microscopic origin of this behavior.

We first analyze the correlations between the minimum in L_{pq}/L_{pp} and the modification of the hydrogen bond structure of water. Figure 6 shows the oxygen−hydrogen (OH) and oxygen−
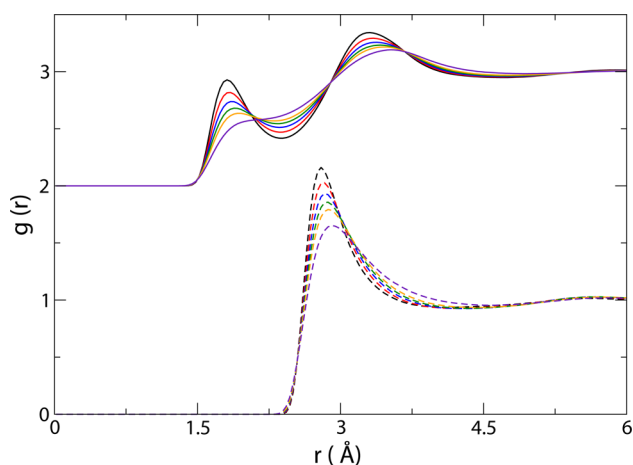

Figure 6. OH and OO radial distribution functions for constant pressure (2000 atm) shown as solid and dashed lines, respectively. The OH data have been shifted upward by 2 units for ease of comparison. The colors have the same meaning as in Figure 5 left.

oxygen (OO) radial distribution functions. These functions do show a reduction in the characteristic hydrogen bond structure, as shown by the disappearance of the characteristic OO secondary peak, and the weakening of the OH first peak with temperature (Figure 6). Moreover, the radial distribution functions show that for the isobar under investigation, 2000 atm, the hydrogen bonded structure is disrupted, but the modification of the structure varies monotonically with temperature. Hence we cannot establish a clear correlation between these structural changes and the minimum in L_{pq}/L_{pp} reported above.

To gain a more quantitative understanding of the modifications in the hydrogen bond structure, we have computed the average number of hydrogen bonds per molecule, N_{HB}, and the tetrahedral order parameters, S_{tet} (Table 2). To define the hydrogen bond, we considered both distance and angle criteria. Two water molecules α and β are hydrogen bonded if the intermolecular oxygen vector $O_\alpha - O_\beta$ is less than 3.5 Å and if the O−O vector falls angularly within 30° of the $O_\alpha - H_\alpha$ vector of a given molecule α. The angular cutoff is consistent with the maximum vibrational amplitude perpendicular to the hydrogen bond, which follows from neutron scattering experiments,[39] and with the critical angle for breaking of hydrogen bonds found in computer simulations.[40] To quantify the tetrahedral order, we have computed the angular order parameter introduced in ref 41

$$S_{tet} = \frac{3}{32} \sum_{i=1}^{3} \sum_{j=i+1}^{4} \left(\cos \phi_{ij} + \frac{1}{3} \right)^2$$

(12)

where the sum runs over of the four nearest neighbors of a given water molecules and ϕ_{ij} is the angle between two "bonds" joining two of those nearest neighbors. The order parameter is normalized, $0 < S_{tet} < 1$, the lower limit, 0, is reached for perfect tetrahedral order and the upper limit, 1, when the bonds are superimposed on each other. An intermediate value, 1/4, corresponds to bonds that are completely uncorrelated.

Our values for N_{HB} feature a large drop with temperature, from 2.81 to 1.05 in going from 500 to 1000 K (Table 2), clearly showing a weakening of hydrogen bonding structure. The tetrahedral order parameter, S_{tet}, is consistent with this idea, increasing from 500 to 1000 K. The values at low temperature indicate the existence of orientational correlations, whereas at high temperature these have disappeared, as can be inferred from the values of S_{tet}, which are larger than the values typical of atomic liquids, 0.15, where no tetrahedral order is present. This dramatic loss of hydrogen bond structure in going from 500 to 1000 K is connected to the large change in water density, which also leads to a significant rise in the diffusion coefficient, approximately 1 order of magnitude in the 500−1000 K interval (Table 2).

The hydrogen bonding structural changes discussed above are expected to influence the heat transport in water as well as the dynamic behavior responsible for the polarization response. *But the fact that all these structural changes are monotonic*, does not provide an obvious correlation between the hydrogen bonding and the ratio L_{pp}/L_{pq}, as the latter does feature a nonmonotonic dependence with temperature. Moreover, the minimum in L_{pp}/L_{pq} appears at ∼725 K, where the hydrogen bonding structure is already significantly disrupted.

To gain more insight into the microscopic origin of the minimum in L_{pq}/L_{pp}, we have estimated the individual phenomenological coefficients, L_{pq} and L_{pp}. The former coefficient determines the coupling between the heat flux and the polarization, whereas the latter quantifies the time decay of the dipolar correlations in the fluid, and it is connected to the Debye relaxation time. To estimate these coefficients and their temperature dependence, we follow de Groot and Mazur[9] and eq 7. We used equilibrium simulations to calculate the Debye relaxation time, τ, and the dielectric constant, ε_r, at the relevant thermodynamic states. We performed both canonical and microcanonical simulations to obtain these quantities. We found that the results were independent of the ensemble used, within the accuracy of our simulations. The Debye relaxation time was obtained from the dipole moment autocorrelation function, $\langle \mathbf{P}(t) \cdot \mathbf{P}(0) \rangle$. The correlation function was subsequently fitted to the double exponential function, $y = A \exp(t/\tau_1) + B \exp(t/\tau_2)$, where the larger of the two decay coefficients is assumed to be that of the Debye relaxation time (τ). Indeed, in all cases the weighting is highly in favor of the function with the longer time scale decay (see Table 2 for the calculated values of τ).

The second phenomenological coefficient, L_{pq}, was then extracted from the ratio, L_{pq}/L_{pp}. We note that in our approach we assume that the response of the fluid to the thermal gradient is linear, and therefore the phenomenological coefficients are independent of the thermal gradient. Our results follow the linear response hypothesis (see, e.g., Figure 4); hence, this assumption is justified.

F

dx.doi.org/10.1021/jp408485d | *J. Phys. Chem. B* XXXX, XXX, XXX−XXX

Figure 7 shows the temperature variation of the phenomenological coefficients as a function of temperature. L_{pp} features a
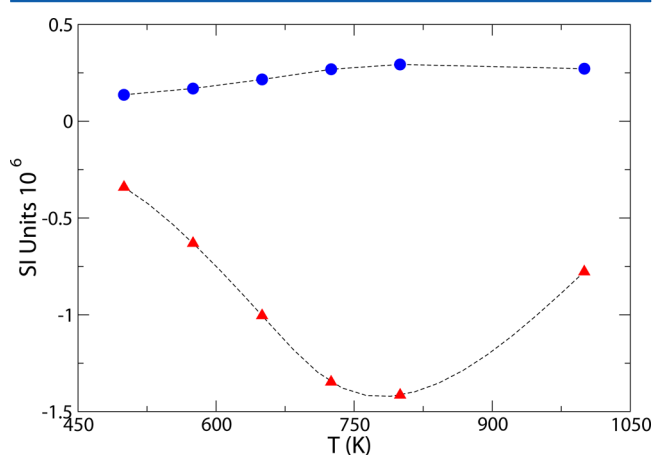

Figure 7. Phenomenological coefficients, L_{pq} in (C K)/ms (red triangles circles) and L_{pp} in (C^2 K)/(J ms) (blue circles) as a function of temperature for the 2000 atm systems.

maximum, which is largely dictated by the ratio $(\varepsilon_r - 1)/\tau$ that features a maximum at around $T \sim 800$ K. This extremum is amplified in the case of the cross coefficient, L_{pq}, which shows a minimum at about the same temperature, indicating that at $T \sim 800$ K the cross correlation between the heat flux and the polarization is strongest. The analysis of the individual coefficients provides microscopic insight on the origin of the maximum thermopolarization response shown in Figure 5. The nonmonotonic behavior in L_{pp} is determined by the dipolar fluctuations, the dielectric constant, and the dipolar relaxation as measured by the Debye relaxation time, and by the different decay rate with temperature of these two functions. Ultimately, the strength of the thermal-polarization response of water will depend on the degree of coupling of the heat flux and the polarization correlations, which are quantified through the L_{pq} coefficient. These cross-correlations can be quantified by computing the Fourier transform, i.e., the power spectrum, of the heat flux and polarization correlation functions. These Fourier transforms provide relevant information on the density of states as well as the characteristic frequencies of the microscopic modes taking part in heat transport and polarization. These power spectra were computed from the autocorrelation functions (ACF) of the quantity (γ) of interest as follows,

$$S_\gamma(\nu) = \int_0^\infty \langle \gamma(t)\,\gamma(0) \rangle_n \cos(\nu t)\,\mathrm{d}t \qquad (13)$$

where the terms in parentheses are the corresponding time correlation functions for the heat flux, the polarization, and the hydrogen velocity (see below). The heat flux was computed using the corresponding microscopic equation for the heat flux (see, e.g., ref 25). The subscript n in the correlation function indicates that we have used the normalized correlation function such that $\int_0^\infty S_\gamma(\nu)\,\mathrm{d}\nu = 1$. In using the cosine term for the transform, we have taken advantage of the fact that our system is classical, and that the correlation functions are symmetric and real.

Figure 8 shows the corresponding power spectra. The polarization power spectrum displays the characteristic exponential decay at long times, thus leading to a Lorentzian type power spectra with a peak at low frequencies, which decreases
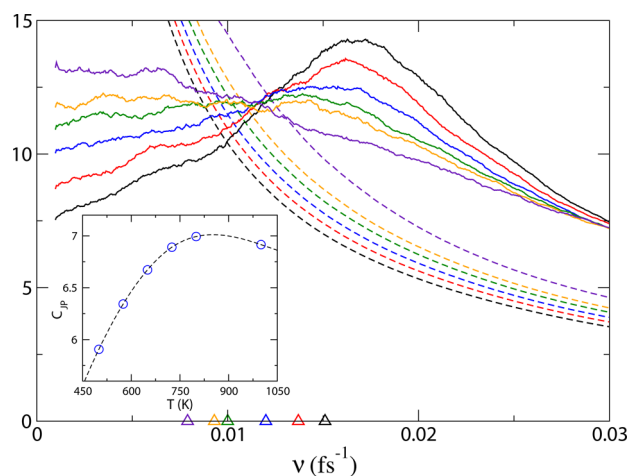

Figure 8. Normalized power spectrum of the heat flux and polarization correlation functions in inverse, $1/\nu$, units. Temperatures have the same color key as previous figures, ranging from 500 K (black) to 1000 K (purple). The inset shows the cross-correlation of the heat flux and the polarization, calculated as explained in the text. The triangles represent the positions of the primary peak in the power spectra of the hydrogen velocity autocorrelation function and are meant to aid a rough comparison between these maxima and the maxima in the heat-flux density of states.

with increasing temperature. We observe a redistribution of the density of states, with an increase in the intensity of higher frequency modes, typically in the range 10−30 ps^{-1}, which as we will show below is a significant frequency region for the coupling of the heat flux and polarization. The increase of the intensity at higher frequencies can be explained using a simplified Debye model, for which the dipole correlation function decays exponentially, and the decay rate is determined by the Debye relaxation time, $\exp(-t/\tau)$. The Fourier transform of this function is given by, $\tau/(1 + \tau^2\omega^2)$ for $(\tau, \omega) \in \mathbf{R}$, which implies that the intensity is higher at higher frequencies as the correlation time, τ, decreases, i.e., as the temperature increases in our case (Table 2).

The heat flux power spectrum undergoes more complex and distinctive changes as the temperature increases. At low temperatures, it features a broad maximum whose peak is located between 15 and 20 ps^{-1}, showing the existence of a dominant mode in the heat transport process. This frequency region is connected to the rotational reorientations, i.e., librational modes of the water molecules in the cage formed by hydrogen bonded molecules. This idea can be tested by computing the power spectra of the hydrogen velocity autocorrelation function, which shows the librational peak at about the same frequency as the maximum observed in the heat flux correlation function (cf. Figures 8 and 9). The heat flux power spectra show that the librational modes do play a significant role in determining the heat transport at lower temperatures, $T \sim 500$ K.

The librational mode should be sensitive to the environment around a given molecule, in particular, the degree of hydrogen bonding and local density. Indeed, the density of water at this pressure decreases from 0.931 g/cm^3 at 500 K to 0.468 g/cm^3 at 1000 K. Similarly, the amount of hydrogen bonds per molecule drops from $N_{HB} = 2.81$ to $N_{HB} = 1.05$ in going from 500 to 1000 K (Table 2). This reduction in hydrogen bonding can be seen in the snapshots represented in Figure 9, and it can also be readily seen from simulation trajectories that at lower temperatures the
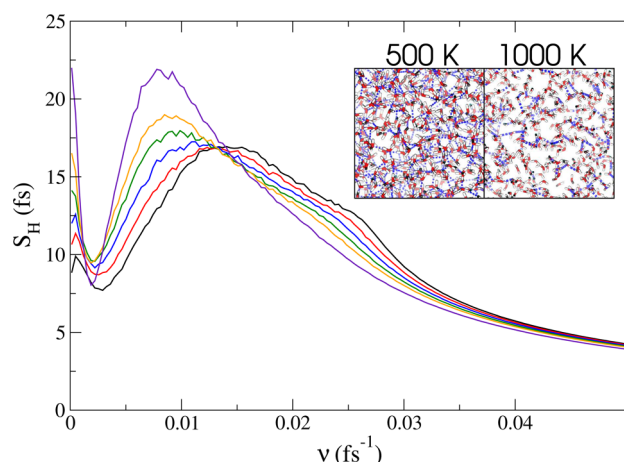
Figure 9. Density of states of the hydrogen velocity autocorrelation functions for the simulated temperatures ranging from 500 K (black) to 1000 K (purple). The broad peak corresponds to the librational modes and is clearly seen to shift to lower frequencies with increasing temperature. The inset shows two simulation snapshots (500 and 1000 K) depicting the hydrogen bonds (shown as dashed blue lines). The hydrogen bonds where constructed using the cutoff criteria discussed in the main text.

rotational dynamics of water molecules is largely restricted by the formation of hydrogen bonds, resulting in reorientational motions between hydrogen bonded configurations. In contrast, at higher temperatures the molecular motion becomes almost free rotating and thus of lower frequency. This shift in frequency is corroborated at 1000 K, with the librational mode moving toward lower frequencies, ~ 8 ps^{-1} (Figure 9). At this high temperature the heat flux does not show clear librational peaks. Hence, our results indicate that the librational mode becomes much less relevant in determining the heat transport at 1000 K. Indeed, heat transport through librations should be more effective at high densities, where molecules are close to each other. However, at 1000 K the density is reduced significantly (0.468 g/cm^3); hence exchange of energy between neighbors, which are more scarce than at higher densities/low temperature, becomes less efficient, and other modes, particularly translational diffusion should become more important in transporting heat.

So far we have shown that the density of states of the polarization power spectrum increases at high frequencies with increasing temperature. On the other hand, the water librational modes contributing to the heat flux power spectrum, shift to lower frequencies as the temperature increases, and the density of states of the heat flux at lower frequency modes increases with temperature. These opposing tendencies of the polarization and the heat flux density of states with temperature, leads to a maximum overlap of the two density of states at intermediate frequencies, ~ 12.5 ps^{-1} and intermediate temperatures, which results in an enhancement of the correlations between the polarization and the heat flux modes. To make these conclusions more clear and to estimate the temperature of maximum overlap of both densities of state, we have computed the cross correlation of the polarization and the heat flux power spectra,

$$C_{JP} = \int_0^\infty S_{J_q}(\nu) \, S_P(\nu) \, d\nu \tag{14}$$

The cross-correlation, see inset in Figure 8, increases with temperature and reaches a maximum at about 800 K. This temperature agrees very well with the temperature at which we

observe the minimum in the L_{pq} cross coefficient. Hence the maximization of the heat flux and polarization coupling as measured by L_{pq}, is connected to a maximum overlap of the polarization and heat flux density of states.

IV. CONCLUSIONS AND FINAL REMARKS

In this paper we have investigated the dependence of the thermal-polarization response of water with the thermodynamic state using nonequilibrium molecular dynamics (NEMD) simulations and the widely used SPC/E model. We have recently shown that this model provides a good description of thermal transport of water at liquid and supercritical conditions, and it reproduces the thermal-polarization effect first observed with the modified central force model of water. The NEMD algorithm implemented in this work has been tested by computing the thermal conductivity of water. We find excellent agreement between the results obtained in this work and those reported in previous investigations. Preliminary investigations with a flexible version of the SPC/E model also support the existence of the thermal polarization in water.

Our results confirm previous estimates on the magnitude of the polarization field induced by the thermal gradient. The ratio of phenomenological coefficients, L_{pp}/L_{pq}, which determines the magnitude of the thermal-polarization response lies between 1 and 6 V for a wide range of thermodynamic states. Hence, thermal gradients of the order of 10^{6-8} K/m, which can be achieved using current experimental setups, should lead to polarization fields of order 10^{4-6} V/m. These fields are small but they could lead to thermophoretic velocities of the order of 10^2 μm/s, which may be relevant at small scales (micrometer or smaller).

The strength of the thermal-polarization response depends on the thermodynamic state conditions. We find that the strength decreases with increasing pressure, and interestingly, it shows a nonmonotonic dependence with temperature, featuring a maximum at specific thermodynamic states. This is an important result as it demonstrates the possibility of maximizing the thermal-polarization response by tuning the temperature and pressure. This idea is also important to direct future experiments aimed at quantifying the thermal-polarization response of water.

To explain the microscopic origin of the thermal-polarization response, we have performed a systematic analysis of the hydrogen bonding structure of water in the relevant range of pressures and temperatures. We do not find a clear correlation between hydrogen bonding structure and the thermal-polarization response. However, the analysis of the individual phenomenological coefficients, L_{pp} and L_{pq}, has been shown to be more informative. To compute these coefficients, we made use of a relationship derived by de Groot and Mazur, which connects the coefficient L_{pp} with the dielectric constant, temperature and Debye relaxation time of the system. The L_{pp} coefficient features a small maximum, whereas $|L_{pq}|$ is maximized at the temperature where we observe the maximum thermal-polarization response, giving strong evidence that these responses are linked to the cross correlations of the heat and polarization fluxes. The existence of this strong correlation should be relevant in determining the thermal conductivity of water. It is known that nonequilibrium coupling effects have an impact on the thermal conductivity. According to non-equilibrium thermodynamics, the stronger the coupling the lower the thermal conductivity and the entropy production (see ref 11 for a discussion of this effect in the context of thermal polarization). Such effects have also been discussed in the context

of thermoelectric effects in molten salts[42] where the impact of the coupling on the thermal conductivity can be very significant, ~40% and much higher. Hence, the thermal conductivity of water, when it is polarized by the thermal gradient, should be reduced with respect to the nonpolarized cases, or in other words the coupling of the field and the thermal gradient would modify the heat flux with respect to the value without coupling. Moreover, the polarization should have an impact on the fluid static dielectric constant providing a possible route to measure the effect.

The approach we have followed to obtain the phenomenological coefficients provides the right qualitative behavior for these coefficients with the thermodynamic conditions, but to quantify the thermal conductivity from these coefficients, an accurate approach that does not assume a Debye model, might be needed, as the thermal conductivity is very sensitive to the magnitude of the coefficients. Further investigation in this direction is therefore required and will be tackled in future works.

Finally, we have investigated the microscopic origin of the maximization of the thermal-polarization effect. The polarization enhancement can be traced back to the correlations between the heat flux and the sample dipole dynamic correlations. A density of states analysis reveals that the water librational modes contribute significantly to the water heat transport mechanism. An increase in the temperature of the sample results in a redistribution of the density of states of the heat flux. We find a red shift in the frequency of the librational modes with increasing temperature. This shift leads to an enhancement of the low frequency modes at high temperatures and low densities. At the same time an increase in temperature enhances high frequency modes in the density of states of the polarization correlation function. We have shown that these opposite tendencies, namely a shift to lower frequencies in the heat flux and to higher frequencies in the polarization, lead to a maximum overlap of the density of states of these two quantities at a temperature that corresponds to the maximum coupling of the heat and polarization fluxes as indicated by the L_{pq} phenomenological coefficient. Our work thus shows that the thermal polarization of water can be tuned by modifying the dynamic correlations of the heat flux and the sample total dipole moment. This conclusion should apply to other polar fluids that should feature the thermal-polarization effect discussed here.

■ AUTHOR INFORMATION

Corresponding Authors
*J. Armstrong: e-mail, j.armstrong@imperial.ac.uk.
*A. Lervik: e-mail, anders.lervik07@imperial.ac.uk.
*F. Bresme: e-mail, f.bresme@imperial.ac.uk.
Notes
The authors declare no competing financial interest.

■ ACKNOWLEDGMENTS

■ REFERENCES

(1) Debuschewitz, C.; Köhler, W. Molecular Origin of Thermal Diffusion in Benzene Plus Cyclohexane Mixtures. *Phys. Rev. Lett.* **2001**, *87*, No. 055901.

(2) Wiegand, S. Thermal Diffusion in Liquid Mixtures and Polymer Solutions. *J. Phys.: Condens. Matter* **2004**, *16*, R357−R379.

(3) Artola, P.; Rousseau, B. Microscopic Interpretation of a Pure Chemical Contribution to the Soret Effect. *Phys. Rev. Lett.* **2007**, *98*, No. 125901.

(4) Duhr, S.; Braun, D. Why Molecules Move Along a Temperature Gradient. *Proc. Natl. Acad. Sci. U. S. A.* **2006**, *103*, 19678−19682.

(5) Rasauli, S.; Golestanian, R. Soret Motion of a Charged Spherical Colloid. *Phys. Rev. Lett.* **2008**, *101*, No. 108301.

(6) Würger, A. Transport in Charged Colloids Driven by Thermoelectricity. *Phys. Rev. Lett.* **2008**, *101*, No. 108302.

(7) Jiang, H.; Wada, H.; Yoshinaga, N.; Sano, M. Manipulation of Colloids by a Nonequilibrium Depletion Force in a Temperature Gradient. *Phys. Rev. Lett.* **2009**, *102*, No. 208301.

(8) Wienken, C.; Baaske, P.; Rothbauer, U.; Braun, D.; Duhr, S. Protein-Binding Assays in Biological Liquids Using Microscale Thermophoresis. *Nat. Commun.* **2010**, *1*, 100.

(9) Groot, S. R. D.; Mazur, P. O. *Non-Equilbrium Thermodynamics*; North-Holland Publishing Co.: Amsterdam, 1962.

(10) Romer, F.; Wang, Z.; Wiegand, S.; Bresme, F. Alkali Halide Solutions Under Thermal Gradients: Soret Coefficients and Heat Transfer Mechanisms. *J. Phys. Chem. B* **2013**, *117*, 8209−8222.

(11) Bresme, F.; Lervik, A.; Bedeaux, D.; Kjelstrup, S. Water Polarization Under Thermal Gradients. *Phys. Rev. Lett.* **2008**, *101*, No. 020602.

(12) Lehmann, O. Structur, System und magnetisches Verhalten flussiger Krystalle und deren Mischbarkeit mit festen. *Ann. Phys. (Leipzig)* **1900**, *307*, 649−705.

(13) Dolgikh, A.; Kosov, D. Out-of-equilibrium one-dimensional disorder dipole chain. *Phys. Rev. E* **2013**, *88*, No. 012118.

(14) Muscatello, J.; Römer, F.; Sala, J.; Bresme, F. Water under Temperature Gradients: Polarization Effects and Microscopic Mechanisms of Heat Transfer. *Phys. Chem. Chem. Phys.* **2011**, *13*, 19970−19978.

(15) Armstrong, J.; Bresme, F. Water polarization induced by thermal gradiente: The extended simple point charge model (SPC/E). *J. Chem. Phys.* **2013**, *139*, No. 014504.

(16) Römer, F.; Bresme, F.; Muscatello, J.; Bedeaux, D.; Rubí, J. Thermomolecular Orientation of Nonpolar Fluids. *Phys. Rev. Lett.* **2012**, *108*, No. 105901.

(17) Govorov, A.; Zhang, W.; Skeini, T.; Richardson, H.; Lee, J.; Kotov, N. Gold nanoparticle ensembles as heaters and actuators: melting and collective plasmon resonances. *Nanoscale Res. Lett.* **2006**, *1*, 84−90.

(18) Barreiro, A.; Rurali, R.; Hernandez, E.; Moser, J.; Pichler, T.; Forro, L.; Bachtold, A. Subnanometer motion of cargoes driven by thermal gradients along carbon nanotubes. *Science* **2008**, *320*, 775−778.

(19) Bresme, F. Equilibrium and Nonequilibrium Molecular-Dynamics Simulations of the Central Force Model of Water. *J. Chem. Phys.* **2001**, *115*, 7564−7574.

(20) Berendsen, H. J. C.; Grigera, J. R.; Straatsma, T. P. The Missing Term in Effective Pair Potentials. *J. Phys. Chem.* **1987**, *91*, 6269−6271.

(21) Römer, F.; Lervik, A.; Bresme, F. Nonequilibrium Molecular Dynamics Simulations of the Thermal Conductivity of Water: A Systematic Investigation of the SPC/E and TIP4P/2005 Models. *J. Chem. Phys.* **2012**, *137*, No. 074503.

(22) http://lammps.sandia.gov/.

(23) Wolf, D.; Keblinski, P.; Phillpot, S.; Eggebrecht, J. Exact method for the simulation of Coulombic systems by spherically truncated, pairwise r^1 summation. *J. Chem. Phys.* **1999**, *110*, 8254−8282.

(24) Fennell, C.; Gezelter, J. Is the Ewald Summation Still Necessary? Pairwise Alternatives to the Accepted Standard for Long-range Electrostatics. *J. Chem. Phys.* **2006**, *124*, No. 234104.

(25) Muscatello, J.; Bresme, F. A Comparison of Coulombic Interaction Methods in Non-Equilibrium Studies of Heat Transfer in Water. *J. Chem. Phys.* **2011**, *135*, No. 234111.

(26) Neumann, M. Dipole moment fluctuation formulas in computer simulations of polar systems. *Mol. Phys.* **1983**, *50*, 841−858.

(27) Zahn, D.; Schilling, B.; Kast, S. Enhancement of the Wolf Damped Coulomb Potential: Static, Dynamic, and Dielectric Properties of Liquid

Water from Molecular Simulation. *J. Phys. Chem. B* **2002**, *106*, 10725–10732.

(28) Bedrov, D.; Smith, G. Thermal conductivity of molecular fluids from molecular dynamics simulations: Application of a new imposed-flux method. *J. Chem. Phys.* **2000**, *113*, 8080–8084.

(29) Zhang, M.; Lussetti, E.; de Souza, L.; Müller-Plathe, F. Thermal Conductivities of Molecular Liquids by Reverse Nonequilibrium Molecular Dynamics. *J. Phys. Chem. B* **2005**, *109*, 15060–15067.

(30) Evans, W.; Fish, J.; Keblinksi, P. Thermal Conductivity of Ordered Molecular Water. *J. Chem. Phys.* **2007**, *126*, No. 154504.

(31) Sirk, T.; Moore, S.; Brown, E. Characteristics of Thermal Conductivity in Classical Water Models. *J. Chem. Phys.* **2013**, *138*, No. 064505.

(32) Hafskjold, B.; Ikeshoji, T.; Ratkje, S. On the Molecular Mechanism of Thermal-Diffusion in Liquids. *Mol. Phys.* **1993**, *80*, 1389–1412.

(33) Bresme, F.; Hafskjold, B.; Wold, I. Nonequilibrium Molecular Dynamics Study of Heat Conduction in Ionic Systems. *J. Phys. Chem.* **1996**, *100*, 1879–1888.

(34) Hockney, R. W.; Eastwood, J. W. *Computer Simulation Using Particles*; Adam Hilger: New York, 1989.

(35) Huber, M.; Perkins, R.; Friend, D.; Sengers, J.; Assael, M.; Metaxa, I.; Miyagawa, K.; Hellmann, R.; Vogel, E. *J. Phys. Chem. Ref. Data* **2012**, *41*, No. 033102.

(36) National Institut of Standards and Technology, NIST Chemistry WebBook. http://webbook.nist.gov/chemistry/.

(37) Alejandre, J.; Tildesley, D. J.; Chapela, G. A. Molecular dynamics simulation of the orthobaric densities and surface tension of water. *J. Chem. Phys.* **1995**, *102*, 4574–4583.

(38) Guissani, Y.; Guillot, B. A computer simulation study of the liquid-vapor coexistence curve of water. *J. Chem. Phys.* **1993**, *98*, 8221–8235.

(39) Teixeira, J.; Bellisent-Funel, M.-C.; Chen, S.; Dianoux, A. Experimental determination of the nature of diffusive motions of water molecules at low temperatures. *Phys. Rev. A* **1985**, *31*, 1913–1917.

(40) Impey, R.; Madden, P.; McDonald, I. Spectroscopic and transport properties of water model calculations and the interpretation of experimental results. *Mol. Phys.* **1982**, *46*, 513–539.

(41) Chau, P.-L.; Hardwick, A. J. A New Order Parameter for Tetrahedral Configurations. *Mol. Phys.* **1998**, *93*, 511–518.

(42) Salanne, M.; Marrocchelli, D.; Merlet, C.; Ohtori, N.; Madden, P. Thermal conductivity of ionic systems from equilibrium molecular dynamics. *J. Phys.: Condens. Matter* **2011**, *23*, No. 102101.